# Proton angular distribution following multiphoton dissociative ionization of $H_2$

S. Yang and W. T. Hill III
*Institute for Physical Science and Technology, University of Maryland, College Park, Maryland 20742*
(Received 19 September 1994)

The angular distribution of protons ejected following resonant (2+1)-photon dissociative ionization of $H_2$ by 193-nm radiation through the $E,F$ state has been obtained. The analysis shows that the Π character of the degenerate continuum states is approximately eight times larger than the Σ character, which is consistent with previous single-photon measurements. The analysis presented here, together with a previous analysis of the proton energy distribution, reveals the ionization channel to be significantly stronger than both the dissociation and dissociative ionization channels.

PACS number(s): 33.80.Rv, 33.80.Gj, 33.80.Eh, 33.80.Wz

## I. INTRODUCTION

Resonant multiphoton excitation in diatomic systems offers a unique opportunity to study competition between ionization and dissociation channels not possible in single-photon experiments. This is due to the simple fact that the wave function describing the intermediate state can be very different from that describing the ground state. In a previous paper we demonstrated how the distribution of final products, ions and neutrals, can be manipulated by a judicious choice of the intermediate state [1]. Specifically, in a (2+1)-photon process through the $E$ state ($H_2$) or $F$ state (HD), the third photon excited continua at either short ($H_2$) or large (HD) internuclear distances. We observed that when the intermediate state wave function was localized in the $E$ well, the fragments originate primarily from states built upon the $1s\sigma_g$ core of $H_2^+$. On the other hand, when the intermediate state wave function was localized in the $F$ well, we observed an increase in the products originating from states built on the $2p\sigma_u$ core. Whereas in our previous study we focused on the energy distribution of protons (a measure of the intensity) of the various channels, in this paper we will turn our attention to their angular distribution, which lifts the degeneracy between Σ and Π continuum states. Our analysis of the angular distribution, together with our previous analysis of the energy distribution, provides the evidence necessary to conclude that resonant (2+1)-photon excitation at 193 nm leads primarily to $H_2^+$.

## II. EXPERIMENT

The apparatus employed in this study was nearly the same as that described in Refs. [1,2]. A broadband ($\Delta\lambda \sim 100$ cm$^{-1}$) ArF* excimer laser composed of an oscillator and an amplifier was used to produce 70% linearly polarized 12-ns pulses with a peak focused intensity of $\sim 5\times10^{10}$ W/cm$^2$ at 193 nm (6.4 eV). The experiment was performed in a vacuum chamber that housed an ion time-of-flight (TOF) detector used to measure the number of each fragment produced and its kinetic energy. The ion detector consisted of extraction and acceleration regions (20 and 100 V/cm, respectively), a 30-cm field-free drift tube, and a pair of microchannel plates (MCP). The detector collected ions over a solid angle of $1.5\times10^{-3}$ sr with a temporal resolution of 1 gigasample/s to give an energy resolution of about ±12%, 0.3 eV at 2.5 eV. Figure 1 shows a typical proton TOF spectrum with the polarization axis of the laser aligned with the TOF axis. It consists of fast and slow protons. The slow protons are in the peak marked $S$. The peaks marked with $F$ and $B$ contain the fast protons initially directed toward and away from the detector, respectively. Figure 2 shows the relative proton yield versus initial kinetic energy obtained by converting the proton TOF into kinetic energy and correcting for the energy-dependent collection efficiency [1,3].

To measure the angular distribution of the ionic fragments, we mounted two rotatable fused silica Brewster windows inside the amplifier cavity of the laser. This provided a way to rotate the polarization direction relative to the TOF axis. This method also accounts for the

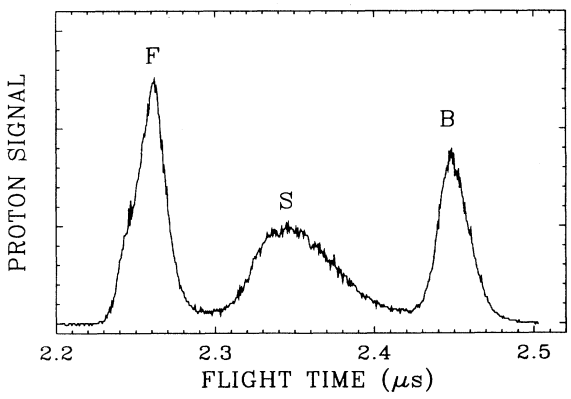


FIG. 1. Typical TOF broadband proton spectrum composed of 64 laser shots. The peaks marked by $F$, $B$, and $S$ indicate fast forward, fast backward, and slow proton components, respectively (see text). Operating conditions: TOF axis aligned with the laser polarization direction ($\Theta=0°$); extraction field is 20 V/cm, acceleration field is 100 V/cm, and front MCP plate voltage is 1900 V.

 

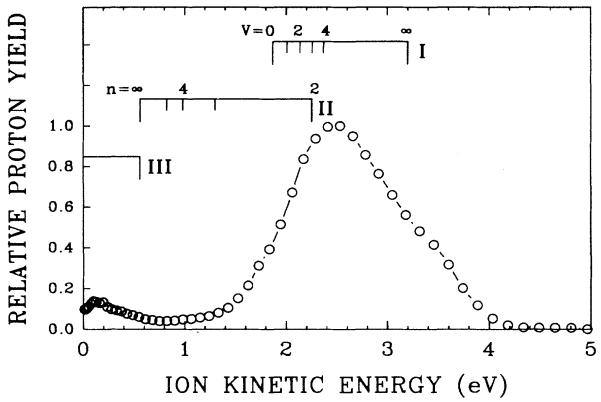


FIG. 2. Relative proton yield vs initial kinetic energy. The trace corresponds to the TOF spectrum of Fig. 1 but has been corrected for the collection efficiency of the TOF detector as discussed in Ref. [1]. The templates above the trace indicate the allowed ranges for the ionization (I), dissociation (II), and dissociative ionization (III) channels (see text).

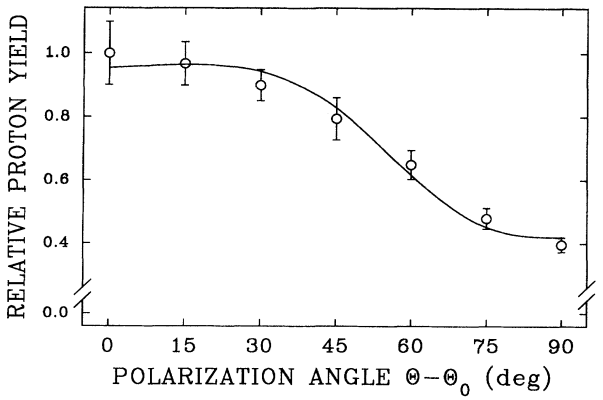


FIG. 3. Relative proton yield for the fast protons (channels I and II) vs polarization angle. The open circles and vertical bars are the mean value and standard error of the yield taken from eight measurements (each similar to Fig. 1) for each angle. The solid curve is the fit to Eq. (30) with $\Theta$ being the angle between the laser polarization and the TOF detector and $\Theta_0$ ($=13.2°$) the shift of $\Theta$ determined by the fit.

modest polarization of only 70%. A TOF spectrum was obtained every 15° between 0° and 90° with a $H_2$ pressure of $(3-4)\times10^{-6}$ Torr. Since ions were collected over such a small solid angle, we were able to determine the number of fast ions at the various angles without correcting for the flight time dependence on angle. Figure 3 shows the number of fast protons ejected along the TOF axis as a function of angle between the $E$ vector of the laser and the TOF axis.

The kinetic energy represented by each peak was determined by computer simulations (as outlined in Refs. [1,2]) using the fact that the forward and backward going components have different flight times. Specifically, the difference in flight times $\Delta t$ gives

$$E(\text{eV})=9.649\times10^{11}\frac{(qV_{12}\Delta t)^2}{(8l_{12}^2M)}\ , \tag{1}$$

where $q$ is the number of electron charges on the ion, $M$ is the mass of the ion (in amu), $l_{12}$ is the length of the extraction region (in cm) and $V_{12}$ is the voltage applied across the extraction region (in volts).

## III. DISSOCIATIVE IONIZATION OF $H_2$

Before analyzing the angular distribution in Fig. 3, it is worthwhile reviewing the interpretation of Fig. 2. A detailed analysis of dissociative ionization is presented in Ref. [1]. It showed that there are three distinct fragmentation channels that are influenced by the $E,F\,{}^1\Sigma_g^+(v=6,J=0)$ state (see Fig. 4) [4]. These channels are labeled channel I, three-photon ionization,

$$H_2(X)\underset{2h\nu}{\rightarrow}H_2(E,F)\underset{h\nu}{\rightarrow}H_2^+(X)+e^-\ , \tag{2}$$

channel II, three-photon dissociation,

$$H_2(X)\underset{2h\nu}{\rightarrow}H_2(E,F)\underset{h\nu}{\rightarrow}H(1s)+H(nl)\ , \tag{3}$$

with $n\geq2$ and channel III, dissociative ionization (i.e., excitation of $H_2$ into the continuum of the $2p\sigma_u$ state of $H_2^+$),

$$H_2(X)\underset{2h\nu}{\rightarrow}H_2(E,F)\underset{h\nu}{\rightarrow}H(1s)+H^+ +e^-\ . \tag{4}$$

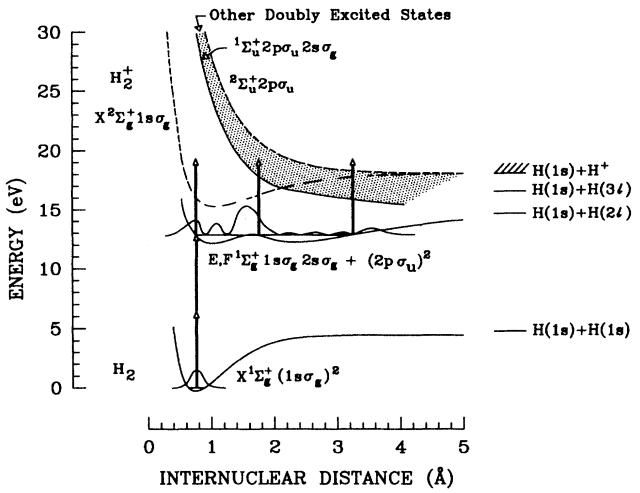


FIG. 4. Selected potential curves of $H_2$ and $H_2^+$. The solid and dashed curves correspond to Sharp's calculation of the neutral and molecular ion, respectively [13]. The doubly excited states converging to the $^2\Sigma_u^+(2p\sigma_u)$ state of $H_2^+$ are located in the dotted region between the $^1\Sigma_u^+(2p\sigma_u2s\sigma_g)$ and $^2\Sigma_u^+(2p\sigma_u)$ curves and are taken from Guberman's calculation [14]. Several neutral dissociation thresholds are indicated to the right of the molecular curves. The arrows represent the transitions induced by 6.4-eV (193-nm) photons. The three originating at the $E,F$ state (from the left to the right) indicate the ionization (channel I), dissociation (channel II), and dissociative ionization (channel III) regions, respectively. The vibrational wave function for the $v=6$ level of the $E,F$ state as well as that for the $X$ state are also sketched in the figure [5].

Each channel leads to a characteristic proton energy spectrum. For channel I, a fourth photon produces protons through dissociation,

$$h\nu+H_2^+(X)\rightarrow H(1s)+H^+, \tag{5}$$

with kinetic energies ranging from 1.88 to 3.20 eV depending on the vibrational level of the molecular ion generated via Eq. (2). For channel II, the excited hydrogen atoms are ionized,

$$h\nu+H(nl)\rightarrow H^+ +e^- , \tag{6}$$

to produce protons with kinetic energies ranging from 0.56 to 2.25 eV depending on the principal quantum number of the excited atomic state. For channel III, no additional photons are required to produce protons with energies between 0 and 0.56 eV.

The allowed ranges of kinetic energies for the channels are indicated in Fig. 2. We note from Fig. 2 that (i) channels I and II have overlapping proton spectra and thus cannot be distinguished from the proton kinetic energy spectrum alone, while the spectrum of channel III is isolated and (ii) the contribution from channel III is small compared with that of channels I and II—it contributes less than 7% to the entire proton yield. As discussed in Ref. [1], this is due to the fact that the wave function of the $v=6, J=0$ level of the $E,F$ state of $H_2$ is more localized in the inner $E$ well with a $1s\sigma_g 2s\sigma_g$ configuration [5,6]. In the absence of coherence in the excitation or correlated electronic motion to reduce the cross section, the dominant transitions in a single-particle picture are expected to be to states built upon the $H_2^+(1s\sigma_g)$ core:

$$h\nu+H_2(1s\sigma_g 2s\sigma_g)\rightarrow H_2^+(1s\sigma_g)+e^-(\epsilon l\lambda) . \tag{7}$$

When the $v=7$ vibrational level of the $E,F$ state is excited, which is more localized in the $F$ well, channel III makes a larger contribution [1]. The dominant single-electron transitions from the $F$ well, with a $2p\sigma_u^2$ configuration, would be to states built upon a $H_2^+(2p\sigma_u)$ core:

$$h\nu+H_2(2p\sigma_u^2)\rightarrow H_2^+(2p\sigma_u)+e^-(n,\epsilon l\lambda) . \tag{8}$$

These would include the doubly excited states that lead to dissociation of $H_2$ ($\rightarrow H+H$ with one of the hydrogen atoms in an excited state, channel II) and dissociative ionization of $H_2$ ($\rightarrow H+H^+ +e^-$, channel III) [1].

## IV. ANALYSIS OF THE PROTON ANGULAR DISTRIBUTION

The angular distribution of the fast proton peak shown in Fig. 3 has a maximum at $\Theta=0°$, where the directions of the electric field of the laser and the TOF axis coincide. Since the rotational energy of the parent molecule prior to dissociation is small ($J\sim 1$) and the translational energy of the departing proton and hydrogen atom is considerably larger ($\sim 2$ eV), the semiclassical axial recoil approximation is valid [7]. This means that the parent molecule, $H_2$ or $H_2^+$, preferentially dissociates along the internuclear axis. Since the production of protons involves several photons, the internuclear axis will be neither parallel nor perpendicular to the polarization direction in general. Consequently, to determine the contribution to Fig. 3 from channels I and II, it is necessary to trace the various paths for each channel one step at a time, which we do below.

It is convenient, in the following analysis, to refer to the laboratory-fixed, $XYZ$, and the rotating molecule-fixed, $xyz$, coordinate systems in Fig. 5. The molecule is oriented along the $z$ axis, while the laser beam is incident along the $X$ axis and polarized along the $Z$ axis. The $XYZ$ frame, as we have defined it, is not fixed in space but, instead, is linked to the polarization vector of the laser. The radiation induces a dipole moment either along the $z$ axis for $\Delta\Lambda=0$ transitions (parallel type) or along the $y$ axis for $\Delta\Lambda=\pm 1$ transitions (perpendicular type) [8]. The unit vectors for these two dipole moments are

$$\begin{aligned}\hat{\boldsymbol{\mu}}_\parallel &= (\sin\theta\cos\phi)\hat{\mathbf{X}}+(\sin\theta\sin\phi)\hat{\mathbf{Y}}+(\cos\theta)\hat{\mathbf{Z}} ,\\ \hat{\boldsymbol{\mu}}_\perp &= -(\cos\theta\cos\phi\sin\psi+\sin\phi\cos\psi)\hat{\mathbf{X}}\\ &\quad -(\cos\theta\sin\phi\sin\psi-\cos\phi\cos\psi)\hat{\mathbf{Y}}+(\sin\theta\sin\psi)\hat{\mathbf{Z}} .\end{aligned} \tag{9}$$

The fragments are collected in the $YZ$ plane at an angle $\Theta$ with respect to the $Z$ axis. This direction is given by

$$\hat{\mathbf{n}}(\Theta)=(\cos\Theta)\hat{\mathbf{Z}}+(\sin\Theta)\hat{\mathbf{Y}} . \tag{10}$$

Both channels leading to the fast proton peak involve a two-photon transition to the bound $E,F$ state and a one-photon transition into the continuum (ionization and dissociation). Since the second step involves only one photon and is less complicated, we will begin with it.

### A. One-photon step

We will first consider the case when a laser is 100% linearly polarized in the $Z$ direction. In the frame of the molecule the transition rate can be written as

$$\hat{\mathbf{R}}(\theta,\phi)=\text{const}\times|\langle f|H|i\rangle|^2 , \tag{11}$$

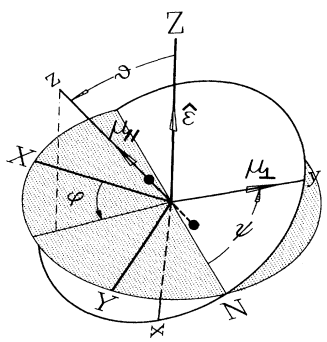


FIG. 5. The space-fixed, $XYZ$, and molecule-fixed, $xyz$, coordinate systems with the $\theta$, $\phi$, and $\psi$ Euler angles indicated. The internuclear axis of the molecule is aligned with the $z$ axis while the laser propagates along the $X$ axis and is polarized along the $Z$ axis.

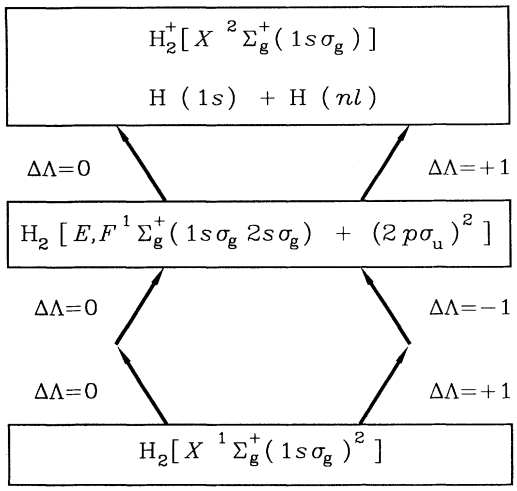


FIG. 6. The four (2+1)-photon excitation paths responsible for the fast protons of channels I and II.

where $H$ is the radiation Hamiltonian. When expressed in the "length" form we can write

$$\hat{\mathbf{R}}(\theta,\phi)=R|\hat{\epsilon}\cdot\hat{\mu}|^2 , \tag{12}$$

where $R$ is the transition rate integrated over all space, $\hat{\epsilon}$ is the polarization direction, and $\hat{\mu}$ is the direction of the induced dipole moment. As discussed above, we have two orientations for $\hat{\mu}$. For $\Delta\Lambda=0$ ($\hat{\mu}_\parallel$) the transition rate takes the form

$$\tilde{R}_\parallel(\theta,\phi)=R_\parallel|\hat{\epsilon}\cdot\hat{\mu}_\parallel|^2=R_\parallel|\hat{\mathbf{Z}}\cdot\hat{\mu}_\parallel|^2=R_\parallel\cos^2\theta , \tag{13}$$

while for $\Delta\Lambda=\pm1$ ($\hat{\mu}_\perp$) we have

$$\begin{aligned}\tilde{R}_\perp(\theta,\phi)&=\frac{R_\perp}{2\pi}\int_0^{2\pi}|\hat{\epsilon}\cdot\hat{\mu}_\perp|^2 d\psi\\&=\frac{R_\perp}{2\pi}\sin^2\theta\int_0^{2\pi}\sin^2\psi\, d\psi=\frac{R_\perp}{2}\sin^2\theta .\end{aligned} \tag{14}$$

For $\Delta\Lambda=\pm1$ transitions, $\hat{\mu}_\perp$ can be anywhere in the $xy$ plane perpendicular to the $z$ axis. Consequently, we must average over all possible orientations ($\psi$) in the plane.

To adjust for the fact that our laser is only 70% polarized, we will treat the unpolarized part as two orthogonal linearly polarized beams with a random relative phase. The transition rates for each polarization take the form

$$\begin{aligned}\bar{R}_\parallel(\theta,\phi)&=\frac{R_\parallel}{2}(|\hat{\mathbf{Z}}\cdot\hat{\mu}_\parallel|^2+|\hat{\mathbf{Y}}\cdot\hat{\mu}_\parallel|^2)\\&=\frac{R_\parallel}{2}(1-\sin^2\theta\cos^2\phi)\end{aligned} \tag{15}$$

and

$$\begin{aligned}\bar{R}_\perp(\theta,\phi)&=\frac{R_\perp}{4\pi}\int_0^{2\pi}(|\hat{\mathbf{Z}}\cdot\hat{\mu}_\perp|^2+|\hat{\mathbf{Y}}\cdot\hat{\mu}_\perp|^2)d\psi\\&=\frac{R_\perp}{4}(1+\sin^2\theta\cos^2\phi) ,\end{aligned} \tag{16}$$

respectively.

In general, for the case where a beam has a degree of polarization $\kappa$ ($\leq1$), the transition rate for $\Delta\Lambda=0$ transitions would be given by

$$R(\theta,\phi)=R_\parallel[\kappa\cos^2\theta+(1-\kappa)(1-\sin^2\theta\cos^2\phi)] \tag{17}$$

and then

$$R(\theta,\phi)=R_\parallel f(\theta,\phi) . \tag{18}$$

Equations (17) and (18) define our angular distribution function, $f(\theta,\phi)$. For $\Delta\Lambda=\pm1$, we have a similar expression,

$$R(\theta,\phi)=R_\perp f(\theta,\phi) . \tag{19}$$

### B. Two-photon step

There are two possible paths, labeled $\Sigma$-$\Sigma$-$\Sigma$ and $\Sigma$-$\Pi$-$\Sigma$, to consider for the two-photon $H_2(E,\ F\ ^1\Sigma_g^+)\leftarrow H_2(X\ ^1\Sigma_g^+)$ transition. It should be remembered that neither path has an intermediate state that is resonant with the radiation wavelength (see Fig. 6). The general two-photon transition rate is given by

$$\begin{aligned}\tilde{R}(\theta,\phi)&=\text{const}\times\left|\sum_j\frac{\langle\Sigma_f|\mathbf{H}_2|\Lambda_j\rangle\langle\Lambda_j|\mathbf{H}_1|\Sigma_i\rangle}{E_j-h\nu_0}\right|^2 g^{(2)}\\&=\text{const}\times\left|\sum_m\frac{\langle\Sigma_f|\mathbf{H}_2|\Sigma_m\rangle\langle\Sigma_m|\mathbf{H}_1|\Sigma_i\rangle}{E_m-h\nu_0}\right.\\&\quad\left.+\sum_n\frac{\langle\Sigma_f|\mathbf{H}_2|\Pi_n\rangle\langle\Pi_n|\mathbf{H}_1|\Sigma_i\rangle}{E_n-h\nu_0}\right|^2 g^{(2)},\end{aligned} \tag{20}$$

where $g^{(2)}$ is the two-photon coherence factor. In the second line, we have separated the $\Delta\Lambda=0$ and $\pm1$ terms. As in the preceding section, we can express the Hamiltonian in the "length" form and write the rate in terms of the transition amplitudes, $c_\alpha(\alpha=\parallel$ for the $\Sigma$-$\Sigma$-$\Sigma$ path or $\alpha=\perp$ for the $\Sigma$-$\Pi$-$\Sigma$ path), as

$$\begin{aligned}\tilde{R}(\theta,\phi)=\frac{g^{(2)}}{4\pi^2}\int_0^{2\pi}\int_0^{2\pi}&|c_\parallel(\hat{\epsilon}_2\cdot\hat{\mu}_{2\parallel})(\hat{\epsilon}_1\cdot\hat{\mu}_{1\parallel})\\&+c_\perp(\hat{\epsilon}_2\cdot\hat{\mu}_{2\perp})(\hat{\epsilon}_1\cdot\hat{\mu}_{1\perp})|^2 d\psi_1 d\psi_2 .\end{aligned} \tag{21}$$

After a considerable amount of algebra, it can be shown that the cross terms cancel. The rates for $\Delta\Lambda=0$ and $\pm1$ are then separable and can be written as

$$\begin{aligned}\tilde{R}_\parallel^{(2)}(\theta,\phi)&=|c_\parallel|^2 g^{(2)}|\hat{\epsilon}_1\cdot\hat{\mu}_{1\parallel}|^2|\hat{\epsilon}_2\cdot\hat{\mu}_{2\parallel}|^2\\&=R_\parallel^{(2)}g^{(2)}f_\parallel(\theta,\phi)\end{aligned} \tag{22}$$

for the $\Sigma$-$\Sigma$-$\Sigma$ path and

$$\begin{aligned}\tilde{R}_\perp^{(2)}(\theta,\phi)&=\frac{|c_\perp|^2 g^{(2)}}{4\pi^2}\int_0^{2\pi}\int_0^{2\pi}|\hat{\epsilon}_1\cdot\hat{\mu}_{1\perp}|^2|\hat{\epsilon}_2\cdot\hat{\mu}_{2\perp}|^2 d\psi_1 d\psi_2\\&=R_\perp^{(2)}g^{(2)}f_\perp(\theta,\phi)\end{aligned} \tag{23}$$

TABLE I. One-photon and two-photon transition rate parameters for 70% linearly polarized excitation beams.

| Two-photon transition type[a] | $f^{(2)}(\theta,\phi)$[b] | $g^{(2)}$ | $\kappa$[c] | One-photon transition type | $f(\theta,\phi)$ | $\kappa$ |
|---|---|---|---|---|---|---|
| $\parallel,(P,P)$ | $C^4$ | 2 | $0.7^2$ | $\parallel,P$ | $C^2$ | 0.7 |
| $\parallel,(P,U)$ or $(U,P)$ | $C^2(1-X^2)/2$ | 3/2 | $0.7\times0.3$ | | | |
| $\parallel,(U,U)$ | $(1-X^2)^2/4$ | 3/2 | $0.3^2$ | $\parallel,U$ | $(1-X^2)/2$ | 0.3 |
| $\perp,(P,P)$ | $S^4/4$ | 2 | $0.7^2$ | $\perp,P$ | $S^2$ | 0.7 |
| $\perp,(P,U)$ or $(U,P)$ | $S^2(1+X^2)/8$ | 3/2 | $0.7\times0.3$ | | | |
| $\perp,(U,U)$ | $(1+X^2)^2/16$ | 3/2 | $0.3^2$ | $\perp,U$ | $(1+X^2)/2$ | 0.3 |

[a] $\parallel=\Delta\Lambda=0$ transition, $\perp=\Delta\Lambda=\pm1$ transition, $P$ denotes linearly polarized photon, $U$ denotes unpolarized photon.
[b] $C=\cos\theta, S=\sin\theta, X=\sin\theta\cos\phi$.
[c] $\kappa$ is the polarization factor: 0.7 for polarized photon and 0.3 for unpolarized photon.

for the $\Sigma$-$\Pi$-$\Sigma$ path. As in the one-photon case, $f(\theta,\phi)$ is the angular distribution.

Before we can evaluate the transition rate, we must consider how coherence will affect the excitation. This information is contained in the two-photon coherence factor $g^{(2)}$. The $g$ factor depends solely on the laser polarization as follows [9]:

$$g^{(2)}=\frac{1}{2}(3+P^2), \quad \text{where } P=\left|\frac{I_\parallel-I_\perp}{I_\parallel+I_\perp}\right| . \tag{24}$$

For two-photon transitions, $g_{zz}^{(2)}=2$ if both photons are polarized along the $Z$ axis and $g_{00}^{(2)}=\frac{3}{2}$ if both photons are polarized randomly. In the case where one photon is polarized along the $Z$ axis and the other is polarized randomly, we can obtain a value for $g_{0z}^{(2)}$ statistically. Namely,

$$g^{(2)}=\sum_i (\text{probability of } g_i)\times g_i^{(2)} . \tag{25}$$

Specifically,

$$\tfrac{1}{2}(3+P^2)=P^2 g_{zz}^{(2)}+(1-P)^2 g_{00}^{(2)}+2P(1-P)g_{0z}^{(2)} . \tag{26}$$

As a result, $g_{0z}^{(2)}=\frac{3}{2}$.

Accounting for the 70% polarization of our laser is more difficult in the two-photon case because of the many different two-photon combinations. To aid in bookkeeping, we present the relevant combinations in Table I from which it is possible to determine the desired rates one at a time.

## V. DISCUSSION

We are now in a position to estimate the branching ratio between the degenerate multiphoton ionization and multiphoton dissociation channels. We will determine these by solving the rate equations for the (2+1)-photon transition. There are four distinct (2+1)-photon excitation paths that lead to $H_2^+$ states that are responsible for the production of the fast protons; they are illustrated in Fig. 6. Without losing the relevant physics, we can simply refer to these molecular ion states collectively as the final level with a population of $N_f$, which can be estimated from rate equations. Our analysis takes into account the contribution from each path such that $N_f=N_a+N_b+N_c+N_d$, where $N_p$ $(p=a,b,c,d)$ is the number of molecular ions generated via each path. It can be shown that the number of molecules oriented with a specific $\theta$ and $\phi$ for each path is given by

$$\begin{aligned}
N_a(\theta,\phi,\tau)&=\tilde{R}_\parallel(\theta,\phi)\tau\tilde{R}_\parallel^{(2)}(\theta,\phi)\tau N_i(\theta,\phi,0)=R_\parallel R_\parallel^{(2)} g^{(2)}\tau^2 f_\parallel(\theta,\phi)f_\parallel^{(2)}(\theta,\phi)N_i(\theta,\phi,0) ,\\
N_b(\theta,\phi,\tau)&=\tilde{R}_\perp(\theta,\phi)\tau\tilde{R}_\parallel^{(2)}(\theta,\phi)\tau N_i(\theta,\phi,0)=R_\perp R_\parallel^{(2)} g^{(2)}\tau^2 f_\perp(\theta,\phi)f_\parallel^{(2)}(\theta,\phi)N_i(\theta,\phi,0) ,\\
N_c(\theta,\phi,\tau)&=\tilde{R}_\parallel(\theta,\phi)\tau\tilde{R}_\perp^{(2)}(\theta,\phi)\tau N_i(\theta,\phi,0)=R_\parallel R_\perp^{(2)} g^{(2)}\tau^2 f_\parallel(\theta,\phi)f_\perp^{(2)}(\theta,\phi)N_i(\theta,\phi,0) ,\\
N_d(\theta,\phi,\tau)&=\tilde{R}_\perp(\theta,\phi)\tau\tilde{R}_\perp^{(2)}(\theta,\phi)\tau N_i(\theta,\phi,0)=R_\perp R_\perp^{(2)} g^{(2)}\tau^2 f_\perp(\theta,\phi)f_\perp^{(2)}(\theta,\phi)N_i(\theta,\phi,0) .
\end{aligned} \tag{27}$$

The parenthetical superscript 2 indicates parameters associated with the two-photon transition and $\tau$ is the pulse length. Values for the angular distribution function ($f_{\parallel,\perp}$) and coherence factor ($g^{(2)}$) are given in Table I for specific transition combinations. We point out that a rate equation approach is valid here because (i) our laser is broadband, (ii) the two-photon transitions in the neutral molecule are relatively weak and not saturated at our intensities, and (iii) the final state is a molecular ion state—free-bound transitions that could repopulate the

neutral states are improbable at our intensities. Consequently, coherence only modifies the angular distribution as discussed in the preceding section and not the total population.

To estimate the branching ratio from our angular distribution measurements, we must evaluate the rates in Eq. (27). It turns out to be sufficient to consider two ratios of rates,

$$r^{(2)}=\frac{R_{\parallel}^{(2)}}{R_{\perp}^{(2)}} \tag{28}$$

and

$$r=\frac{R_{\parallel}}{R_{\perp}} , \tag{29}$$

which can be extracted from a numerical fit to our data. To this end, we first define four combination rates, $R_a=R_{\parallel}R_{\parallel}^{(2)}$, $R_b=R_{\perp}R_{\parallel}^{(2)}$, $R_c=R_{\parallel}R_{\perp}^{(2)}$, and $R_d=R_{\perp}R_{\perp}^{(2)}$ and note that $R_a/R_c=R_b/R_d$. Next, we write an analytical expression for $N_f$ along the detecting direction, $\theta=\Theta$, $\phi=\pi/2$. With the values in Table I and assuming the initial population in the ground state of the neutral molecule is isotropic, additional algebra leads to

$$\begin{aligned}N_f\left[\Theta,\frac{\pi}{2},\tau\right]=N_i\tau^2[&(1.1295R_a+0.0996R_b+0.00727R_c+0.0006R_d)\cos^6\Theta\\&+(0.5245R_a+0.5933R_b+0.0826R_c+0.0101R_d)\cos^4\Theta\sin^2\Theta\\&+(0.0861R_a+0.1650R_b+0.2968R_c+0.0659R_d)\cos^2\Theta\sin^4\Theta\\&+(0.0051R_a+0.0143R_b+0.0499R_c+0.1414R_d)\sin^6\Theta] .\end{aligned} \tag{30}$$

Numerical fits to Eq. (30) yield

$$r^{(2)}=1.7\pm0.6 \tag{31}$$

for the relative strength between the two-photon paths and

$$r=0.12\pm0.06 \tag{32}$$

for the relative strength between the one-photon paths (see Fig. 6).

Since four photons are involved in the production of the fast protons, it is necessary to show that the fourth photon does not affect the orientation produced by the first three photons. For channel I, the first three photons produce $H_2^+$ primarily in low-lying vibrational levels of the $1s\sigma_g$ state [10], while the fourth photon dissociates $H_2^+$ through the $2p\sigma_u$ state. The calculated single-photon dissociation cross section for these levels is of the order of $10^{-18}$ cm$^2$ [11]. At our intensities, the $1s\sigma_g\rightarrow 2p\sigma_u$ transition will be saturated, thus there will be a one-to-one correspondence between the $H_2^+$ orientation and the proton angular distribution. For channel II, the first three photons dissociate $H_2$, producing two neutral atoms, with one in an excited state. The fourth photon ionizes the excited atoms without altering the flight direction by any significant amount. Again, the proton angular distribution will reflect the molecular orientation after the absorption of the first three photons.

A value of 1.7, determined by our fit, for $r^{(2)}$ is not too surprising since there are two $^1\Pi_u$ states at or below the $E,F$ state and only one $^1\Sigma_u$ state. At the same time, the small value for $r$ indicates that the $\Delta\Lambda=0$ transition is nearly ten times weaker than the $\Delta\Lambda=\pm1$ transition for the third photon. The final state before the electron departs would have $\Pi$ character mostly. Since the final $H_2^+$ state is a $\Sigma$ state, the departing electron would have to carry away this angular momentum in the form of a $p$ wave. To the extent that ionization dominates, this would be consistent with single-photon ionization measurements in the 64-nm region in which a $\beta$ parameter of nearly 2 is observed, indicating strong $p$ character [12].

Our data suggest that the dissociation channel (II) is weaker than the ionization channel (I). This deduction is based in part on the fact that the singly excited singlet Rydberg states of the form $1s\sigma_g nl\sigma_u$, $\pi_u$, which asymptotically approach the ground state of $H_2^+$ and couple to $H(1s)+H(nl)$ separated atoms, all lie below the ground state of $H_2^+$. Consequently, excitation to these states from the $E$ state will leave the system well in the dissociation continuum. Such a dissociation would be highly unfavorable since the system would have to go from a state in which the protons have relatively low kinetic energy, in the $E$ well, to one in which they have much higher kinetic energy. It would be more favorable for the electron to carry off the excess kinetic energy while producing a molecular ion in a low vibrational level of the $1s\sigma_g$ state as is observed experimentally [10]. We should emphasize that the $E$ well has nearly the same shape as the $X$ state of $H_2^+$.

Dissociation could originate, however, from the doubly excited Rydberg states with the same separated atom limits (i.e., a ground state hydrogen atom and an excited atom) but asymptotically approaching the $2p\sigma_u$ state of $H_2^+$. With a 6.4-eV photon, the doubly excited states accessible from the $E,F$ state cannot be reached until the internuclear separation places the system near the maximum of the barrier between the $E$ and $F$ wells. Although the lowest of these states is a $\Sigma$ state, there are $\Pi$ states that are also accessible as we move into the $F$ well.

However, one must remember that the probability of finding the system in the $F$ well is small. In fact, the production of slow protons from channel III, which originates from the $F$ well (see Fig. 4) is 13 times weaker than that of the fast protons (see Fig. 2). We also have evidence that suggests that if the doubly excited states are excited, they evidently autoionize more rapidly than they dissociate. This is because if dissociation were to occur, hydrogen atoms produced in states with $n=2-6$ would be ionized with near unit probability at our intensity [1]. We only observe, however, protons coming from low $n(\leq 3$, see Fig. 2) states. Since the slow protons from channel III (dissociative ionization) result from excitation of the $2p\sigma_u$ continuum, which lies above all the doubly excited states of interest, we must conclude that all the doubly excited states can be reached, albeit at different internuclear distances. With the plethora of curve crossings at large $R$ between these doubly excited states, it is likely that dissociation would lead to hydrogen in many different $n$ states, specifically those with higher $n$ states. (Such a statement cannot be made too strongly without knowing the cross section to each state as a function of internuclear distance from the $F$ state.) Consequently, our angular distribution measurements together with the proton energy distribution of Fig. 2 suggest that multiphoton ionization (direct and indirect) of $H_2$ at 193 nm is more likely than multiphoton dissociation.

## VI. CONCLUSION

The wave function describing the nuclear motion of ground state $H_2$ molecules is only partially delocalized when the system passes through the $E,F$ intermediate state. Thus the strengths of the additional open channels, dissociation (channel II), and dissociative ionization (channel III), are weak compared with that of the ionization channel (channel I). This conclusion is based on our analysis of the proton angular distribution that shows the character of the continua excited by the absorption of three 193-nm photons favors $\Pi$ states over $\Sigma$ states by a ratio of 1:0.12.

## ACKNOWLEDGMENTS

We acknowledge helpful discussions with Dr. J. Goldhar, Dr. J. Cooper, and Dr. M. L. Ginter, and technical support from J. Zhu, D. L. Hatten, and Dr. Y. Cui. This work was sponsored by the National Science Foundation through Grant No. PHY 91 06916.

[1] W. T. Hill III, B. P. Turner, S. Yang, J. Zhu, and D. L. Hatten, Phys. Rev. A **43**, 3668 (1991).

[2] B. P. Turner, W. T. Hill III, S. Yang, J. Zhu, A. Pinkas, and L. Bao, Rev. Sci. Instrum. **61**, 1182 (1990).

[3] S. Yang, W. T. Hill III, and S. N. Dixit, J. Chem. Phys. **100**, 6434 (1994).

[4] The $E,F\,^1\Sigma_g^+(v=6,J=1)\leftarrow X\,^1\Sigma_g^+(v=0,J=1)$ transition is also allowed when the laser runs broadband. However, the intensity of the laser is at least an order of magnitude lower for this transition, because of the Schumann-Runge absorption by $O_2$, which coincides with this line.

[5] P. Senn, P. Quadrelli, K. Dressler, and G. Herzberg, J. Chem. Phys. **83**, 962 (1985).

[6] P. Senn and K. Dressler, J. Chem. Phys. **87**, 1205 (1987).

[7] R. N. Zare, Mol. Photochem. **4**, 1 (1972).

[8] The definition of Euler angles in this study follows the convention of quantum mechanics instead of classical mechanics. See J. J. Sakurai, *Modern Quantum Mechanics* (Addison-Wesley, Redwood City, CA, 1985), pp. 171–174.

[9] R. Loudon, *The Quantum Theory of Light*, 2nd ed. (Oxford University Press, New York, 1983).

[10] L. Anderson, G. D. Kubiak, and R. Zare, Chem. Phys. Lett. **105**, 22 (1984).

[11] G. H. Dunn, Phys. Rev. **172**, 1 (1968). For complete tables see Joint Institute for Laboratory Astrophysics, National Bureau of Standards and University of Colorado Report No. 92, 1968 (unpublished).

[12] See, for example, S. Southworth, W. D. Brewer, C. M. Truesdale, P. H. Kobrin, D. W. Lindle, and D. A. Shirley, J. Electron Spectrosc. **26**, 43 (1982).

[13] T. E. Sharp, At. Data **2**, 119 (1971).

[14] S. L. Guberman, J. Chem. Phys. **78**, 1404 (1983).